Chapter 14
Evaluating the Effect of Shaker Placement Optimization Priorities on Multi-Axis Test Results

Risto Djishev, Kieran Elrod, Connor Tasik, Jim DeClerck, Brittany Ouellette, John Schultze, and Shannon Danforth

Abstract Multi-axis vibration testing is capable of emulating field environments more accurately than traditional single-axis testing. However, the presence of multiple shakers introduces challenges in test setup and execution. Optimization algorithms can help researchers select the location and direction of each shaker in a multi-axis test by minimizing an objective function subject to constraints. One example is to select shaker locations that minimize required shaker force (objective) while matching a power spectral density specification at control degrees of freedom (constraint). The solution given by the algorithm is affected by many variables, including the choice of cost and constraints, metrics used for formulating the cost and constraints, and model fidelity and calibration. When these optimized shaker configurations are implemented in a laboratory setup, differences in boundary conditions, shaker and sensor attachment method, and shaker control are likely to affect how the optimization criteria is reflected in the test results. This case study investigates the challenges and benefits of optimizing shaker location by determining shaker placements from an optimization problem, implementing this suggested shaker configuration in a laboratory test, and comparing results to those from an "engineering judgment" testing configuration.

Keywords Shaker placement optimization · MIMO testing · Vibration control · Finite element modeling · Model updating

Introduction

Environmental testing, or the practice of recreating field conditions in a lab setting for qualification of devices prior to operation, is a widely used process across many industries to ensure successful deployment of products or improve the effectiveness of design iterations. Environmental testing in laboratory settings increases safety and cost effectiveness compared to field testing. In military applications, environmental testing is a legal requirement for new products prior to mass production [1].

This study focuses on random vibration testing, which aims to replicate the acceleration power spectra responses that a device would experience in its operational environment. In this field, testing has traditionally been conducted using

Risto Djishev
Department of Mechanical Engineering, Rice University, Houston, TX 77005
e-mail: rd40@rice.edu

Kieran Elrod
Department of Structural Engineering, University of California, San Diego, La Jolla, CA 92093
e-mail: kieranelrod@gmail.com

Connor Tasik
Department of Mathematics, Rose Hulman Institute of Technology, Terre Haute, IN 47803
e-mail: tasikca@rose-hulman.edu

Jim DeClerck
Department of Mechanical Engineering, Michigan Technological University, Houghton, MI 49931
e-mail: jdeclerck@mtu.edu

Brittany Ouellette · John Schultze · Shannon Danforth
Los Alamos National Laboratory, Los Alamos, NM 87545
e-mail: britt@lanl.gov; schultze@lanl.gov; sdanforth@lanl.gov

Alexandra Karlicek et al. (eds.), *Dynamic Environments Testing, Vol. 7*, Conference Proceedings
of the Society for Experimental Mechanics Series, https://doi.org/10.13052/97887-438-0152-8_14

single-axis electrodynamic shakers. Single-axis testing typically involves testing X,Y, and Z specifications sequentially, then combining results from each axis to form a global error metric [2]. Although single-axis testing is commonly applied, it is known to have several issues. Cross-axis (i.e., out-of-axis) responses are a common problem with single-axis testing. These responses are difficult to incorporate into the global error metric and can negatively affect the in-axis response data. Similarly, the practice of securing the device under test to a shaker plate often means that the real boundary conditions of the structure are not well represented [3]. Therefore, an accurately described input vibration spectra may not recreate a realistic response because the system impedance is not representative of the field impedance. Because of the aforementioned issues with single-axis tests replicating the real environment, it is common for over-testing to lead to unnecessary damage in some axes/responses while paradoxically under-testing other axes/responses [3].

To address these problems with single-axis testing, multi-input, multi-output (MIMO) random vibration testing has become more popular for recreating vibration environments. Utilizing multiple shakers rather than a monolithic shaker base can allow for a more accurate recreation of vibration sources, reduce damage associated with over-testing by reducing the overall force needed to excite critical modes, and capture multi-axis response [3]. However, the placement of input sources for these tests is often based on the judgment of individual engineers, varying the effectiveness of MIMO shaker testing from practitioner to practitioner. To address this shortcoming, researchers have begun to implement optimization approaches for selecting shaker locations and directions in MIMO tests [4] [5].

Optimization algorithms for shaker placement often rely on estimates of the system's frequency response functions (FRFs) from either a finite element analysis (FEA) model or experimental modal analysis. The optimization uses these FRFs to predict the response of a system to shaker inputs at particular degrees of freedom (DOFs). Synthesizing FRFs from an FEA model provides the advantages of obtaining FRFs at a finer resolution than is possible with experimental modal analysis. Furthermore, in a pre-test stage where access to the physical system is limited, experimental modal analysis may not be possible. However, FEA models represent idealized versions of the system and do not perfectly represent the system's material properties or boundary conditions. If the FEA model lacks enough similarity to the physical system in its tested state, then the cost and constraints implemented in the optimization algorithm may not be reflected in the hardware test results.

This paper investigates the challenges and benefits of shaker placement optimization for MIMO testing through a case study with the base of the Box Assembly with Removable Component (BARC). We first develop specifications for a random vibration test using measured field data. Next, we create an FEA model of the test assembly and calibrate this model with findings from an impact test. We use the FEA model and specifications to conduct an optimization that minimizes shaker force while matching the specification at chosen control DOFs. We then implement two laboratory tests: One using engineering judgment for determining shaker placement and one using the optimized shaker DOFs. Finally, we compare the control performance, required shaker force, and global system response between the two test configurations. Figure 1 outlines our approach for conducting this case study. The results indicate that despite using a calibrated FEA model on a relatively simple system, differences in system FRFs between model and hardware led to worse test performance from the optimized configuration.

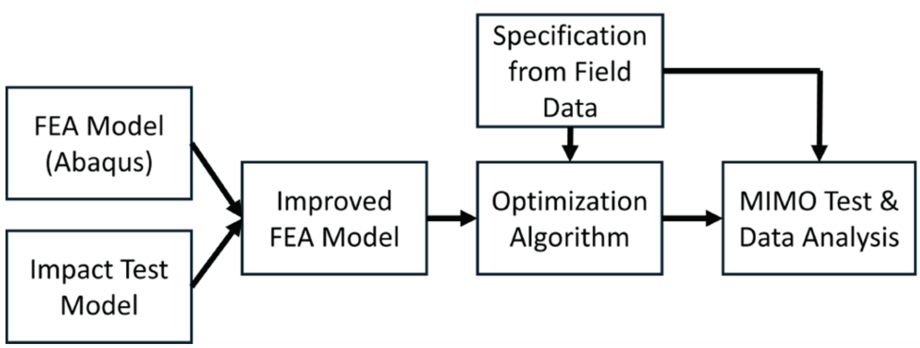

Fig. 1 Flowchart of steps associated with this project.

Environmental Specification

Developing a representative environmental specification is an important step for vibration testing. An overly conservative specification can lead to the accumulation of fatigue damage on potentially irreplaceable components. Conversely, an under-estimate of the vibration environment can lead to critical modes not being excited to the level they would in normal operation. There are several methods for defining a vibration environment depending on the type of loading and the goal of the test. This study focuses on the random vibration associated with a transportation environment.

As noted in the introduction, we used the BARC base as a test article in this study. We instrumented the BARC with triaxial accelerometers, bolted the BARC base to an aluminum plate, and bolted the plate to a metal pallet in a truck bed. The truck was driven around paved and gravel roads for several minutes. We selected two accelerometer channels, 97Z+ and 58X+, to be used as control DOFs for the environmental test. Figure 2 shows the field test setup and sample time data from the two chosen accelerometer channels.

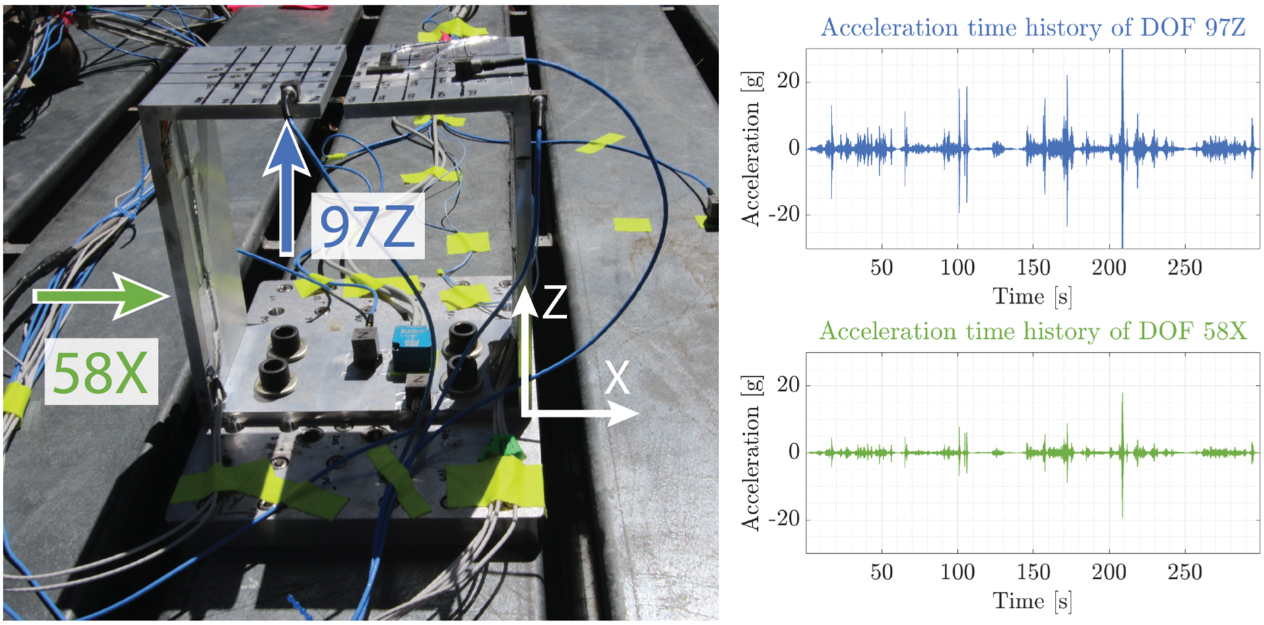

Fig. 2 For field data collection, the BARC base and plate were bolted to a pallet in a truck bed. DOFs 97Z and 58X were chosen as control DOFs, shown on the left, and sample time data from the field test are shown for each DOF on the right.

Random vibration tests are typically controlled to power spectral densities (PSDs) in the frequency domain, which describe the energy present in a signal at each frequency line. Given a time signal $x(t)$, let T denote the period of the signal and h_T denote a function that is equal to one within an arbitrary period and zero elsewhere. Computing $x_T(t) = x(t)h_T(t)$, we produce a signal that is equal to $x(t)$ for one period and zero elsewhere. Let $\hat{x}_T(\omega)$ denote its Fourier transform, with ω indicating a frequency variable. Then, the auto PSD $S_{xx}(\omega)$ is given by

$$S_{xx}(\omega) = \lim_{T\to\infty} \frac{1}{T} |\hat{x}_T(\omega)|^2. \tag{1}$$

To conduct our MIMO environmental test, we developed auto PSD specifications at each of our chosen control DOFs. Cross PSDs are also a consideration in MIMO tests, but we used an in-situ method to define the cross PSDs, described in the Environmental Testing section. Although we did not use the derived cross PSDs from the field data in this study, we did compute them. The Appendix provides more details on the computation and results of the derived cross PSDs.

It is evident from the time data in Figure 2 that the field data contained some minor shocks. Impulses that exceed the average amplitude of the random vibration data would negatively impact the auto-PSD estimation. Furthermore, we planned to use our test software in the Random Vibration configuration, where it is capable of generating only stationary Gaussian-distributed random vibration [6]. Therefore, the data used to generate the specifications needed to match those characteristics [7]. We excluded the shocks present in the data by dividing the time signal into 0.2-second blocks and accepting or rejecting each block using a root-mean-square (RMS) threshold. The value of this threshold was computed based on a P70/50 upper tolerance limit estimation of the RMS amplitudes for each signal block. The 70/50 refers to 50 percent confidence in a 70th percentile upper tolerance limit for the estimated RMS.

Notably, we fit the RMS amplitudes to a normal distribution in the log domain. Working in the log domain allowed for a better fit to a normal distribution, although other distributions were explored. Selection of optimal distributions for RMS rejection is outside the scope of this work, so we decided to primarily focus on normal distributions. These RMS values correspond to the total energy in the time domain signal, so the energy from the shocks would weight individual blocks over the threshold. For a discrete time domain signal $x(t)$ with a set of n values $x_1, x_2, \cdots, x_n$, the RMS is defined as

$$x_{RMS} = \sqrt{\frac{1}{n}(x_1^2 + x_2^2 + \cdots + x_n^2)}. \tag{2}$$

We chose time blocks of 0.2 seconds to keep as much of the testing data as possible, therefore producing a higher level of statistical confidence in our estimate. Figure 3 shows the time signal for DOF 97Z+ and DOF 58X+ with accepted and rejected blocks.

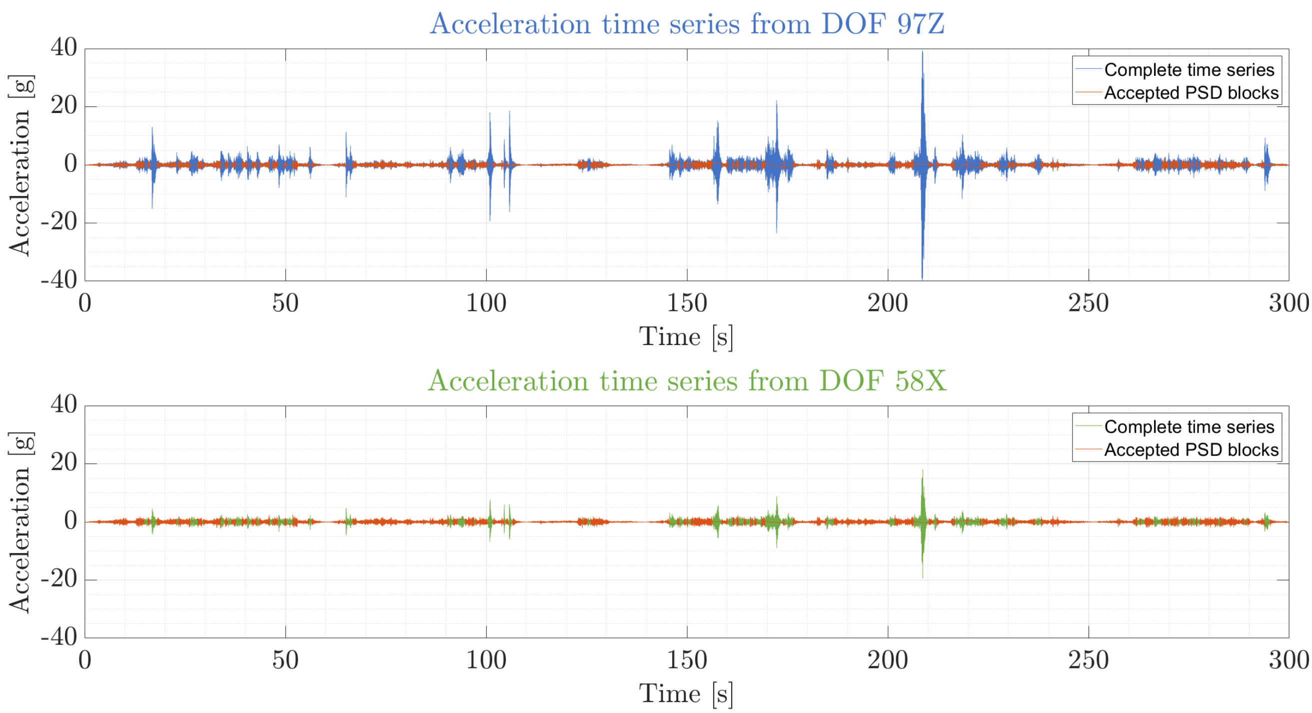

Fig. 3 Time signal for DOF 97Z and DOF 58X with accepted time series blocks.

For each accepted time block, we computed the auto PSDs for DOF 97Z+ and DOF 58X+. We used Welch's power spectral density estimate with the same parameters for each block so that the PSD of each block had values at the same frequency points. In the PSD computation, we used a Hanning window of length 160 points, 50% overlap between segments, and a 160-point discrete Fourier transform. This choice of parameters led to frequency lines with 10 Hz spacing. After examining the auto PSDs, we determined that a test range of 10-800 Hz would be sufficient for our environmental test. Under 10 Hz, the high-displacement vibration could prove a challenge for the small shakers used in this study. Above 800 Hz, the auto PSDs dropped below the noise floor of the accelerometers. Figure 4 shows an example PSD from DOF 97Z, plotted from 10-800 Hz.

We next developed a P95/50 maximum predicted environment (MPE) for each control DOF's auto PSD specification [8]. The 95/50 refers to 50 percent confidence in a 95th percentile upper tolerance limit for the estimated experimental auto PSD. This combination of confidence and tolerance is referred to as a Maximum Predicted Environment (MPE). We assumed a normal distribution for this work because the controller in our laboratory test uses normally-distributed excitation [6] [7]. First, we computed the sample mean $\bar{x}$ and sample standard deviation $\bar{s}$ across N samples. These values are then used to compute the K-factor k_1, an adjustment to the tolerance limit of our normal distribution:

$$a = 1 - \frac{\chi_\alpha^2}{2(N-1)} \tag{3}$$

$$b = \chi_p^2 - \frac{\chi_\alpha^2}{N} \tag{4}$$

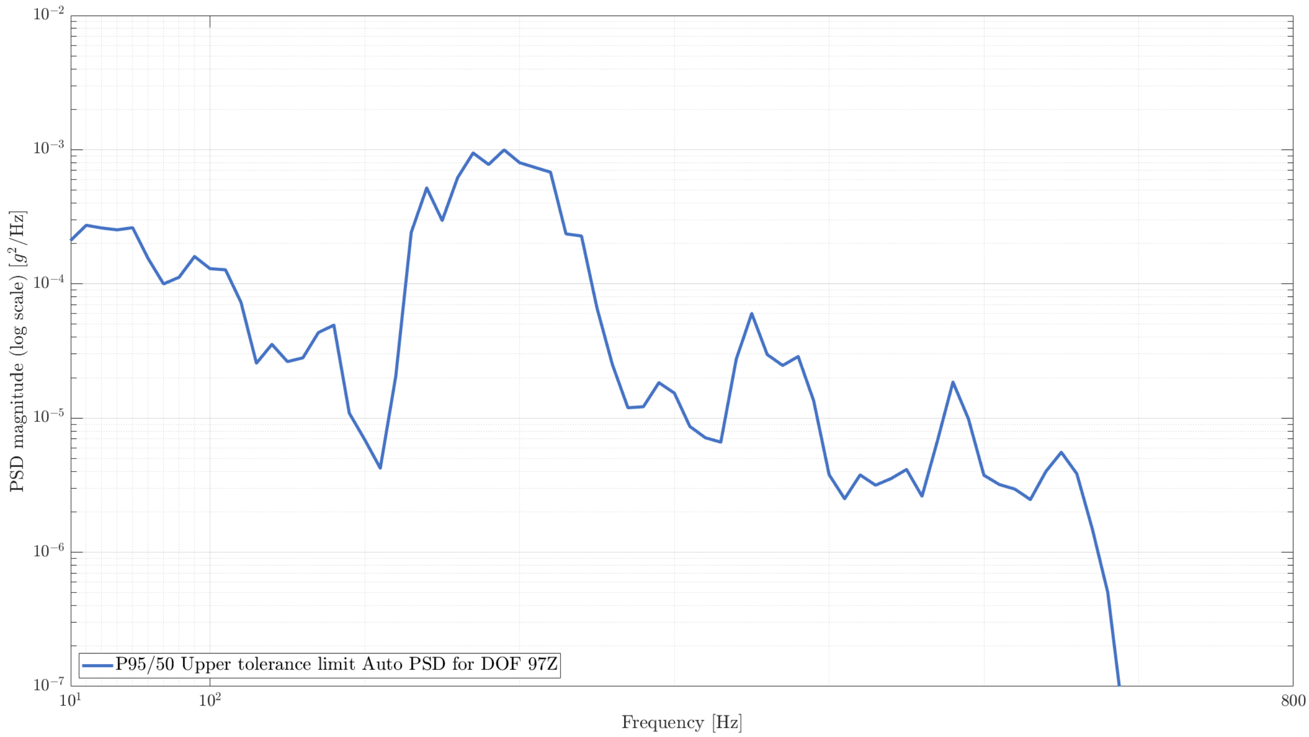

Fig. 4 Representative auto PSD of DOF 97Z from 10 to 800Hz. The drop-off after 700 Hz is due to application of a low-pass digital filter.

$$k_1 = \frac{\chi_p + \sqrt{\chi_p^2 - ab}}{a}, \tag{5}$$

where p is the desired tolerance limit and χ_α is the inverse cumulative distribution function (CDF) of the normal distribution associated with the desired confidence level α with a mean of $\overline{x}$ and a standard deviation $\overline{s}$. The upper tolerance limit Y_U is then given by

$$Y_U = \overline{x} + k_1\overline{s}. \tag{6}$$

Figure 5 shows an example histogram for one control DOF at one frequency line. Figure 6 shows the histogram for the same DOF across all frequency lines.

Finally, we smoothed the auto PSD upper tolerance limit from each channel across several frequency octaves to improve test implementation and to allow the environment to be more generalized [9]. At each octave center point, we took the mean of MPE P95/50 values within one half of an octave. This mean value was used to define the smoothed auto PSD. We interpolated on a log-log plot to find intermediary specification points between octave center point frequency values at a 1 Hz frequency spacing. The PSD vectors were used as the final specification by the MIMO vibration controller and our optimization algorithms.

The final auto PSDs are shown in Figure 7, which also displays the GRMS of the octave-smoothed signal in the title of each subplot. The GMRS, or acceleration RMS in units of earth's gravity g, is a metric describing the energy associated with a given signal. This metric is commonly used in vibration testing to denote relative amplitudes of different random vibration signals. In the frequency domain, the GRMS can be interpreted as the square root of the area under the curve. More formally, the GRMS can be computed from discrete frequency domain signal with a set of M values, given by $\{x_1, x_2, \cdots, x_M\}$ at corresponding frequency lines $\{1, 2, \cdots, M\}$ with frequency spacing f_s:

$$\text{GRMS} = \sqrt{\sum_{i=1}^{M} x_i f_s} \tag{7}$$

We note that by the GRMS metric, each DOF exhibited similar levels of energy in the field test, with DOF 58X slightly higher.

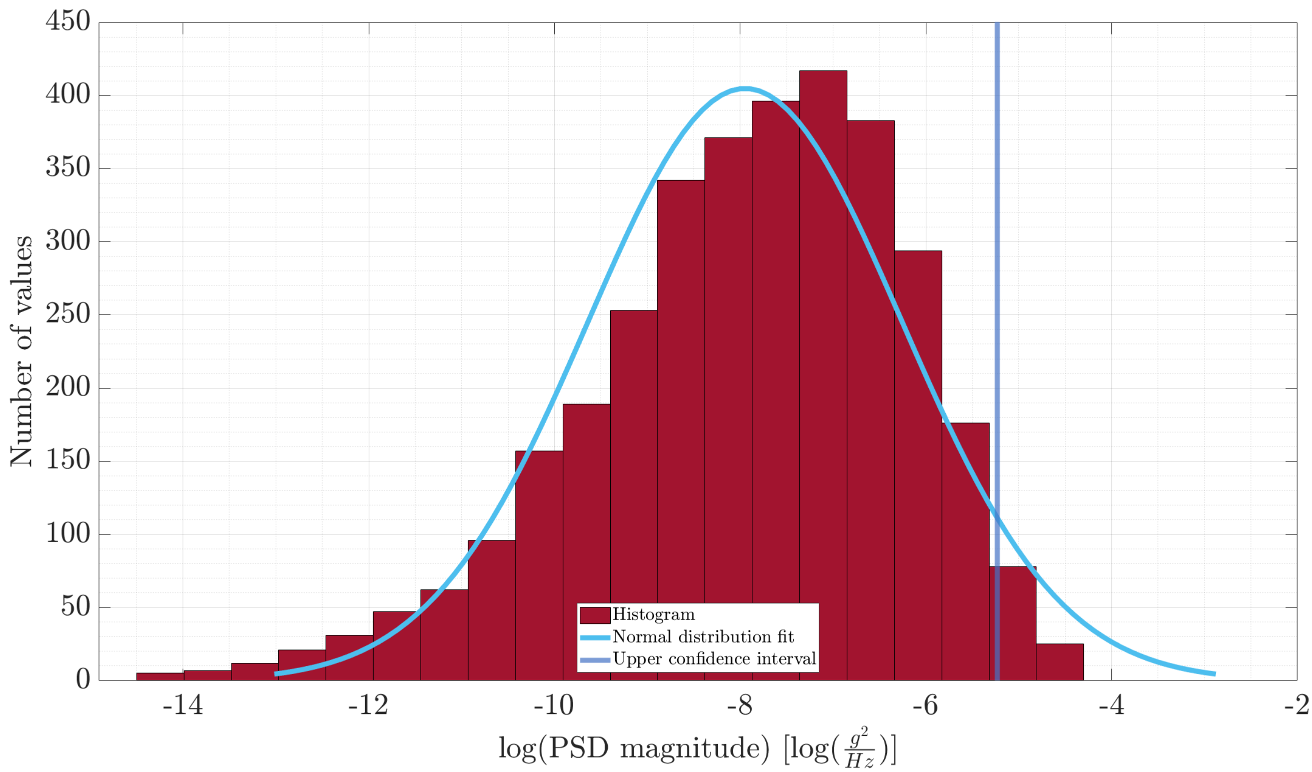

Fig. 5 PSD Magnitude histogram of DOF 97Z at 340Hz.

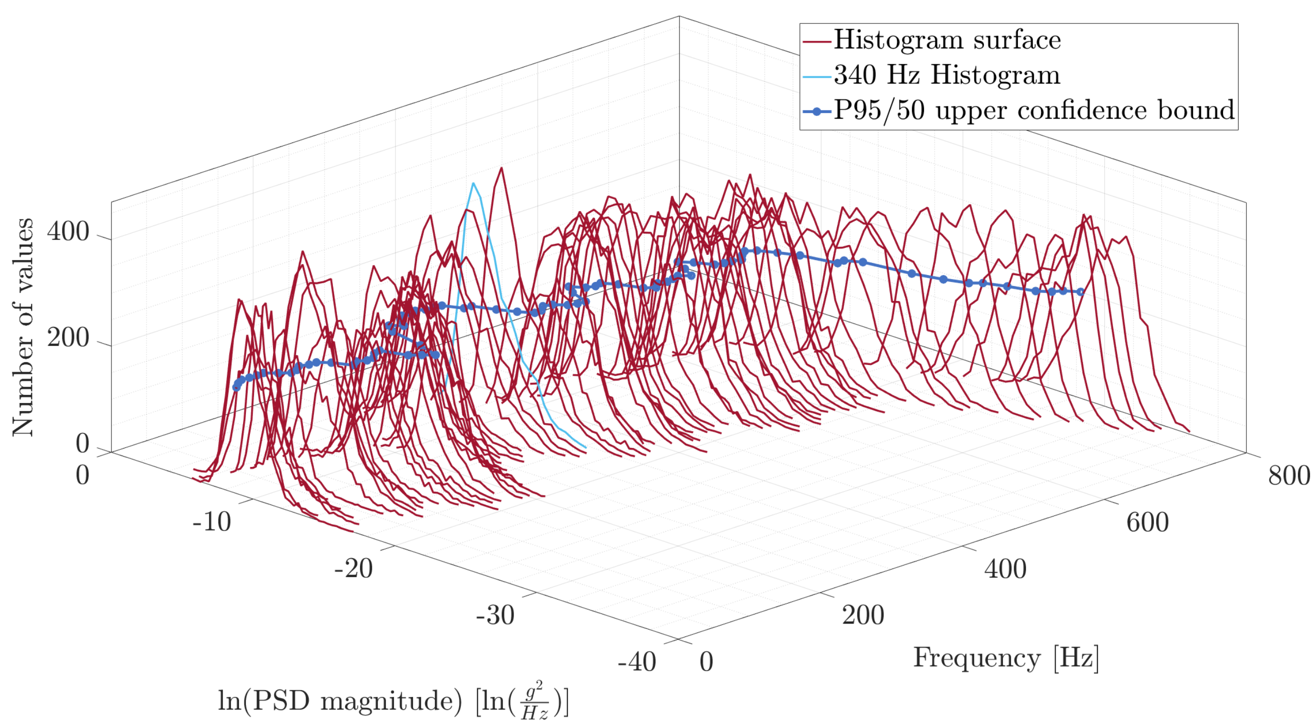

Fig. 6 PSD Magnitude histogram of DOF 97Z across all frequency lines.

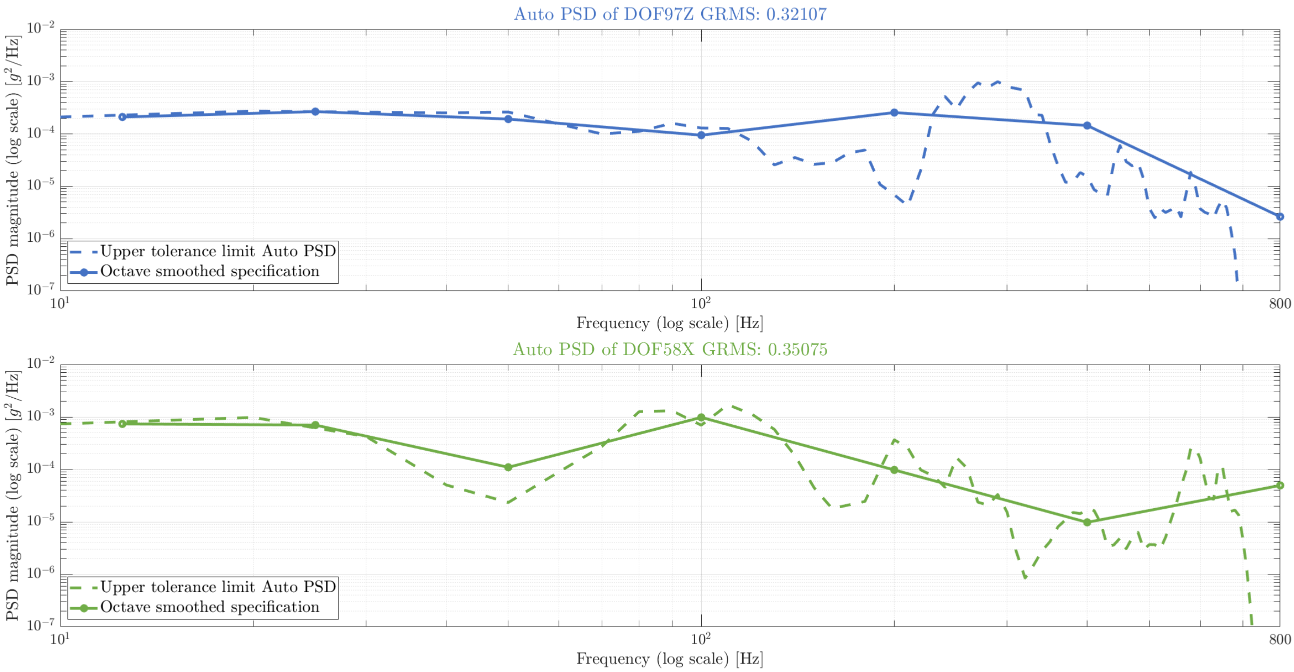

Fig. 7 Final MPE specification Auto PSDs for DOF 97Z and 58X.

Finite Element Analysis and Experimental Modal Analysis

With the specifications created for our environmental test, we next developed and refined a finite element analysis (FEA) model of the BARC base and plate. We created this FEA model to obtain a full set of accelerance frequency response functions (FRFs) for the shaker placement optimization algorithm. We chose a shell model rather than a solid model because previous work found that a shell model of the BARC was less computationally expensive while also producing less error between FEA and experimental modal analyses [10]. The material properties were nominal values for Al6061 (Aluminum), and we kept them consistent for both parts of the assembly.

We used existing engineering drawings and measurements with a ruler and caliper to create the geometry of the BARC base and plate. The shell model did not allow us to vary the diameter of the holes with depth, and since the plate holes included two different diameters, we took the average of them for our modeling. To model the connection between the BARC and plate, our first iteration applied a tie constraint between the circumferences of the bolt holes on the BARC and plate, as seen in Figure 8.

We then performed a mesh convergence study to determine the model's mesh size. We conducted a modal analysis in Abaqus while varying the global seed size from 1/2" to 1/128", reducing the size by a factor of two each time. Once we had computed the system's natural frequencies for each mode of each mesh size, we used Richardson Extrapolation to calculate the theoretical natural frequency of each mode [11]. To determine which mesh to use, we compared the error between the computed natural frequencies from each mesh size to the theoretical natural frequencies. We also considered the computation time for each simulation.

As we reduce the mesh size, we increase the fidelity of the model and expect the frequency values to begin to converge to the theoretical natural frequencies. However, consulting Table 1, we notice that for the lower-frequency modes, the frequency values begin to fluctuate instead of converging around a global seed size of 1/8" and 1/16". We believe this phenomenon is because the mesh becomes fine enough to reach the Abaqus program's noise levels. It is also important to note the simulation time. Computation time is roughly constant down to a global size of 1/16", after which it begins to increase exponentially.

The combination of computation time and fluctuation of natural frequencies prompted us to choose a mesh size of 1/32". The simulation time for this mesh size (81 s) was low enough to allow us to perform many iterations within the study time frame, and the simulated natural frequencies had an error of approximately one tenth of a percent or less when compared to the theoretical natural frequencies from the Richardson Extrapolation (Table 2).

Once we selected our mesh size, we proceeded to simplify the geometry of the assembly while maintaining the original dynamics of the system. We performed a modal analysis in Abaqus for several geometry simplification cases: (A) model the

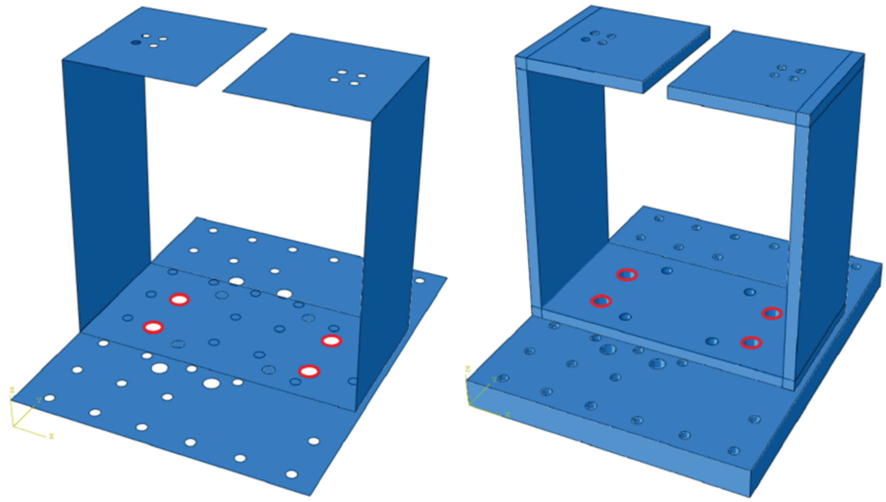

Fig. 8 Initial shell model of the BARC base and plate without the thickness visualized (left) and with the thickness visualized (right).

Table 1 Natural frequencies obtained from the mesh convergence study for each mesh seed size (1/128”-1/2”) and the simulation time.

	Natural Frequencies (Hz)						
Flexural Mode	**Global 1/128”**	**Global 1/64”**	**Global 1/32”**	**Global 1/16”**	**Global 1/8”**	**Global 1/4”**	**Global 1/2”**
1	101.15	101.16	101.17	101.14	101.19	101.17	101.33
2	153.45	153.45	153.45	153.42	153.47	153.45	153.66
3	254.54	254.63	254.80	254.82	255.66	256.03	257.07
4	367.11	367.19	367.34	367.44	368.25	369.03	371.26
5	514.58	514.61	514.69	514.70	515.13	515.39	517.13
6	525.93	526.01	526.18	526.29	527.41	528.83	532.34
7	574.80	574.82	574.89	574.92	575.34	575.71	577.86
8	583.85	584.01	584.34	584.29	586.36	586.92	589.41
Sim Time (sec)	2308	236	81	42	35	33	33

Table 2 Error between Richardson Extrapolation and the 1/32” mesh seed size for each flexural mode.

Flexural Mode	**Richardson Extrapolation Theoretical Natural Frequencies (Hz)**	**Error between 1/32” and Richardson Extrapolation (%)**
1	101.15	0.02
2	153.45	0.00
3	254.53	0.11
4	367.09	0.07
5	514.57	0.02
6	525.90	0.05
7	574.79	0.02
8	583.78	0.10

geometry of all holes in the assembly, (B) Remove all small holes on the plate, (C) Remove all small holes in both parts of the assembly, and (D) Remove all holes except the four main bolt holes connecting the BARC base to base plate. The respective geometries that we considered can be seen in Figure 9. Looking at the results of the FEA modal analysis in Table 3, we

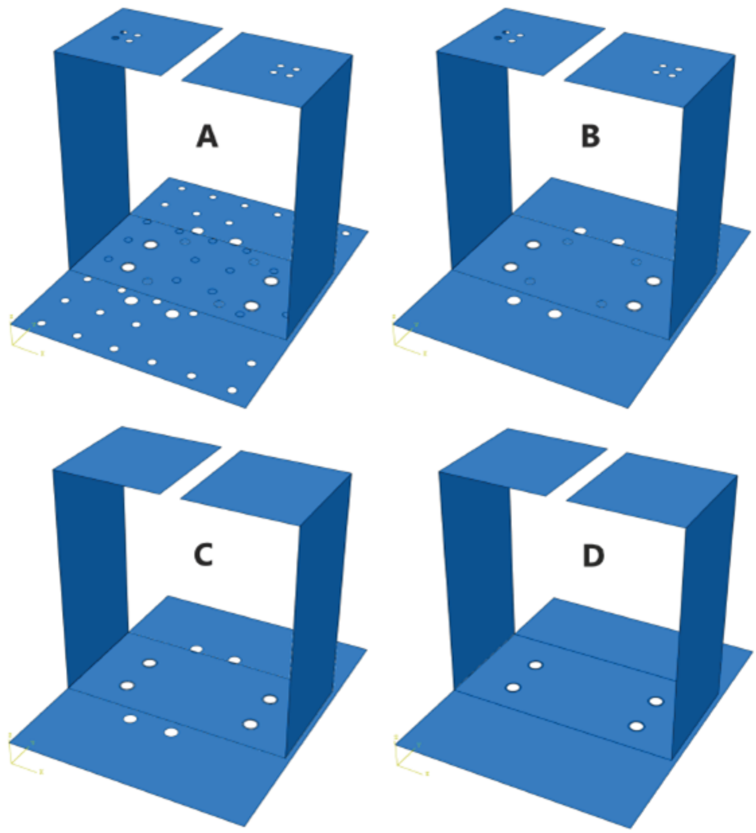

Fig. 9 Different BARC approximations from most detailed (A) to most simplified (D).

Table 3 Natural frequencies for each geometry simplification for the 1/32" mesh size.

	Natural Frequencies (Hz)				
Flexural Mode	**A**	**B**	**C**	**D**	**Error between A and D (%)**
1	101.13	101.17	100.86	100.86	0.27
2	153.92	153.41	153.08	153.02	0.58
3	254.41	254.85	254.38	254.44	0.01
4	368.68	367.24	367.06	366.84	0.50
5	514.86	514.68	515.24	515.17	0.06
6	526.19	526.20	526.38	526.41	0.04
7	575.90	574.80	575.74	575.63	0.05
8	586.40	584.20	584.51	584.18	0.38

notice that the percent difference of the natural frequencies between our most simplified model (D) and the original model (A) are approximately half a percent or less. Given the low difference, we chose option D and simplified the geometry.

After developing the preliminary model, we performed an experimental modal analysis of the assembly using a roving hammer impact test. We suspended the BARC and plate from an aluminum frame using rubber bands and zip ties to simulate the free-free boundary condition which was used in the FEA. We then attached five uniaxial accelerometers to our assembly, with two in the system X and Z axes and one in the Y axis. The accelerometers were exclusively on the BARC component of the assembly because we expected most of the motion to be there based on FEA simulation results and engineering judgment. We then outlined a grid on the assembly consisting of 178 nodes. Ideally, each node would be impacted in all three axes; however, due to the assembly's geometry, some DOFs were impossible to excite. Furthermore, we expected some DOFs to cause the system to act identically due to the symmetry of our assembly. With this in mind, we reduced the number of nodes to 171 and the DOFs to 215. The experimental setup is shown in Figure 10.

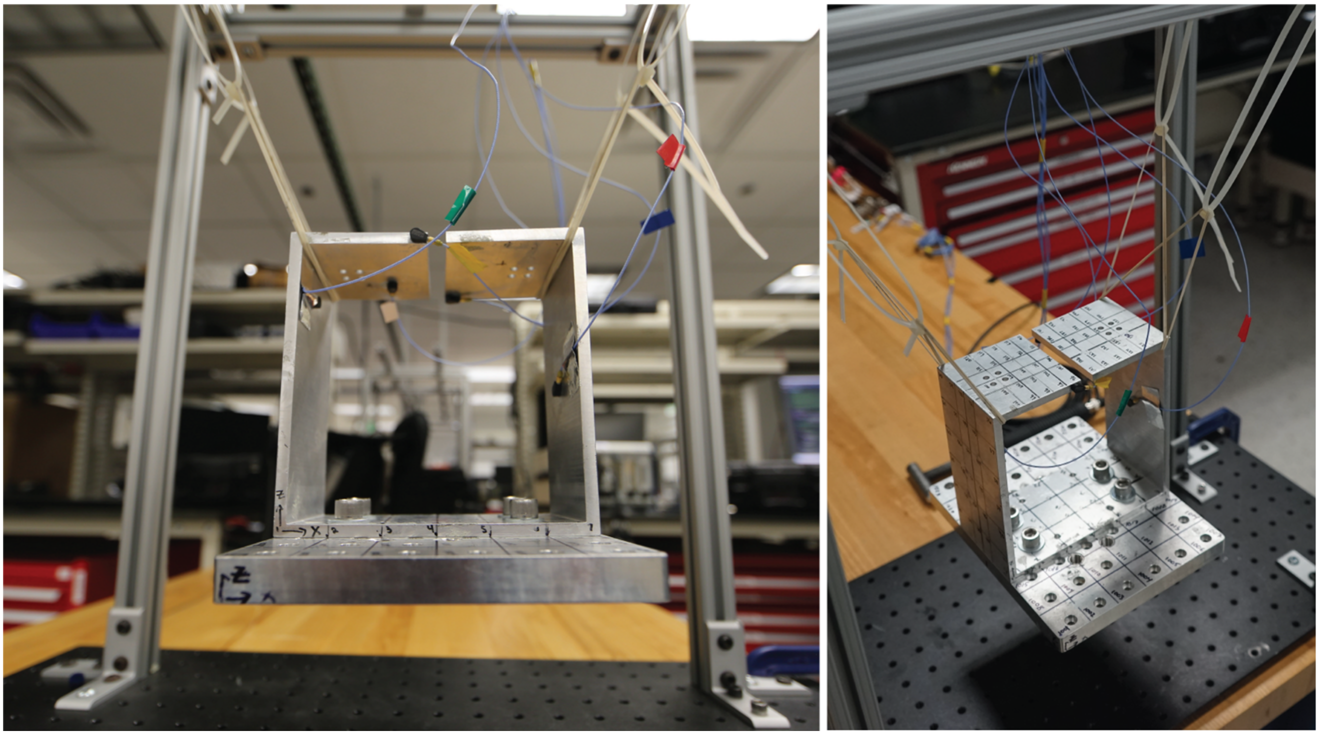

Fig. 10 Two photos of the test setup for experimental modal analysis.

We conducted the testing using Siemens SCADAS Data Acquisition hardware and Simcenter Testlab software, impacting each of the 215 DOFs five times with an instrumented hammer. We processed the impact test data using IMAT, a Matlab toolbox for modal analysis by ATA Engineering. We fit the FRFs using an orthogonal polynomial fitting technique and used these FRFs to obtain natural frequencies and mode shapes of the experimental system.

During the initial comparison between experimental and simulation modal test results, we saw high errors in natural frequency values and observed a mode missing from the experimental test that was present in the FEA results. In reflecting on the large error, we realized that we had made a strong assumption regarding how the plate and the BARC are connected in Abaqus. We also understood that the nonlinear behavior of the contact between the BARC and the base plate would be difficult to model with a linear modal analysis, thus we began to explore various constraint schemes (contact areas) in an effort to best match the experimental modes observed in the impact test. After approximately 40 iterations of tie constraints, we obtained a reasonable result with an average error of 3.13% across the seven modes found in the experimental analysis. Furthermore, the FEA mode shapes qualitatively matched the experimental mode shapes, and the extra mode that was present in the original FEA mode also disappeared with this new model. Note that the number of modes in the frequency range of interest reduced to seven.

Table 4 Natural frequencies for the updated FEA model, the hammer test, and the error between them.

	Natural Frequencies (Hz)		
Flexural Mode	**Hammer Test**	**Updated FEM**	**Error (%)**
1	121.38	117.51	3.19
2	177.13	170.29	3.86
3	315.99	330.64	4.64
4	405.94	402.57	0.83
5	571.44	563.16	1.45
6	643.39	627.27	2.51
7	700.63	662.72	5.41
		Avg Error	**3.13**

The final model's tie constraint is shown in Figure 11. In this final model, we removed all bolt holes, as it simplified the FEA model and produced a lower error on the natural frequencies when compared to experimental results. We attempted other modifications, such as altering BARC and plate thickness and slightly varying the density and modulus of elasticity, but they proved to be ineffective at correcting the frequency errors and the mode shapes.

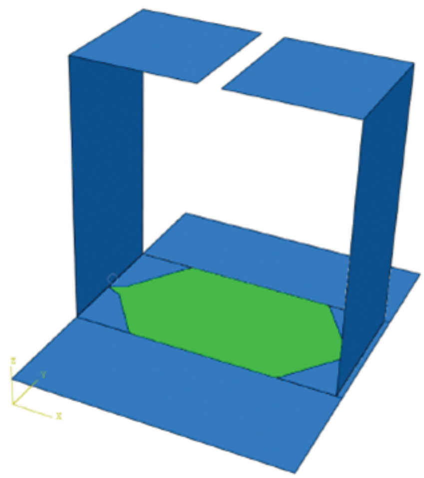

Fig. 11 The final FEA model with the new tie constraint (green area).

Once we were satisfied with the relatively low error as well as the qualitative mode shapes, we performed a Modal Assurance Criterion (MAC) to quantitatively assess mode shape differences between FEA and experiment. The MAC is shown in Figure 12. Modes 1-6 quantitatively match well, but mode 7 has low similarity between FEA and experiment. Figure 12 shows a visual comparison of mode 7 shapes between experimental and FEA analysis. We believe the low correlation could have resulted from poor excitation during the experimental hammer test. However, because mode seven is at 700 Hz, around when the energy in the specifications drops (Figure 4), we decided to proceed with the optimization using this FEA model.

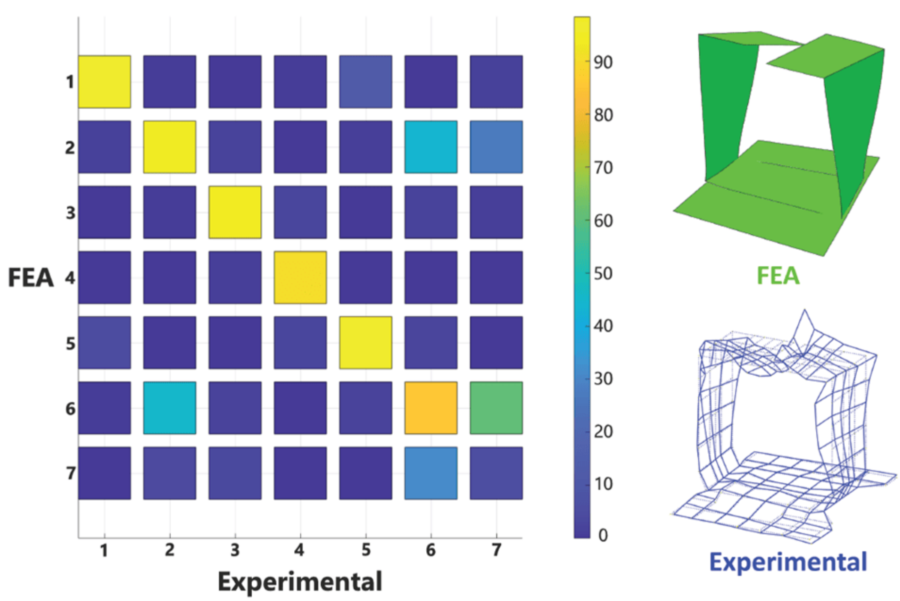

Fig. 12 Modal assurance criterion between the FEA and experimental mode shapes (left) and a visual comparison of mode 7 displacement between FEA and experimental analysis (right).

Shaker Placement Optimization

Distributed shaker vibration tests often pose challenges because the modal shakers used for excitation have a relatively low force input compared to the large shakers used for single-axis testing. Although the environment developed in the Environmental Specification section is a low-level transportation environment, we aimed to develop a testing pipeline that could be generalized for other environments, such as flight. We therefore chose to optimize shaker locations and directions that minimize force to achieve a specified environment. This paper describes an optimization for two shakers because the hardware setup described in the Environmental Testing section only allowed for two outputs. Our optimization aimed to minimize the input force spectrum required by the two shakers to achieve the specification at the two chosen control DOFs.

We imported the geometry, natural frequencies, and mode shapes from the updated FEA model into SDynPy, a structural dynamics Python toolbox developed at Sandia National Laboratories[12]. Each node in the finite element model has three DOFs, which produced too large of a search space for the optimization algorithm. We reduced the search space by selecting a subset of nodes in a 0.25-inch grid, then removing DOFs that were not feasible locations to place a shaker. These candidate DOFs can be seen in Figure 13.

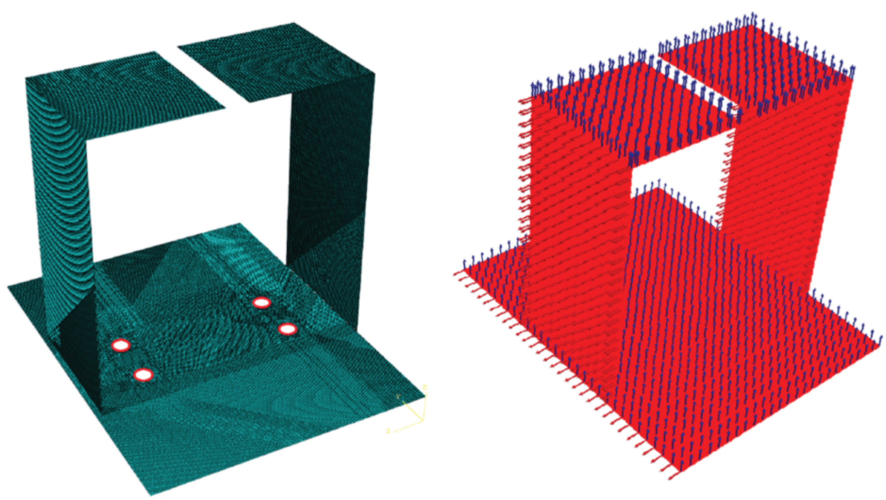

Fig. 13 FEA Model (left) and final set of candidate DOFs with 0.25-inch spacing (right).

Using the system geometry, natural frequencies, and mode shapes in SDynPy, we synthesized FRFs for the BARC system. We imported the MPE auto PSDs developed in the Environmental Specification section, defined as $S_i = [S_{1,i}\ S_{2,i}]^T$ at control DOFs 1 and 2 for each frequency line i ($i \in \{1, 2, \cdots, M\}$ for M frequency lines). At each iteration of the optimization, the algorithm selects two candidate DOFs, given by j and k, as shaker locations. It then computes the synthesized FRF matrix H_i, a 2×2 matrix between the input DOFs (j, k) and the control DOFs $(1, 2)$ for each frequency line i. We use H_i and S_i to compute the required input force spectra $F_i = [F_{j,i}\ F_{k,i}]^T$ to achieve the specification. Our optimization formulation is then given by

$$\begin{aligned}
\min_{j,k} \quad & \sqrt{\sum_{i=1}^{M} F_{j,i} f_s} + \sqrt{\sum_{i=1}^{M} F_{k,i} f_s} \\
\text{s.t.} \quad & S_i = H_i F_i \\
& i \in \{1, 2, \cdots, M\} \\
& j, k \in \{1, 2, \cdots, N\} \\
& j \neq k,
\end{aligned} \tag{8}$$

where N is the number of candidate input DOFs and f_s represents the frequency spacing. Note that the objective function is the sum of force RMS values from each shaker, using the definition of RMS provided in Equation 7. As shown in Equation 8, we added constraints that require the set of candidate DOFs to be a valid set and prohibit the two shaker DOFs from being the same at each iteration.

We implemented this optimization formulation using two solvers from the Python SciPy package: *Brute Force* and *Differential Evolution*. The Brute Force solver searches through every possible combination of candidate DOFs. This strategy finds the globally optimal solution, but it is computationally inefficient. Differential Evolution works with a population of candidate input DOFs. The members of this population are moved around the search space. If a new DOF produces a lower objective function value, then it is accepted back into the population; if it increases the objective function value, then it is discarded. This process is repeated until a satisfactory solution is found. Differential Evolution does not guarantee a globally optimal solution.

Because the optimization used FRFs synthesized from our FEA model, the node numbers in the optimization solution are reported in the FEA model numbering scheme. The Brute Force algorithm produced the candidate set 7X+ and 1929Z+, whereas Differential Evolution found 1937Z+ and 609X+. These DOFs are shown in the middle and right panels of Figure 14, where it can be seen that these solution sets are quite similar. The time to compute these sets, however, differed greatly, with Brute Force taking 10,800 seconds and Differential Evolution taking 73.1 seconds. When mapped onto the coarser experimental grid used for experimental modal analysis, the solution was the same for either solver. Given the similarity in the sets found, we recommend proceeding with Differential Evolution in future work.

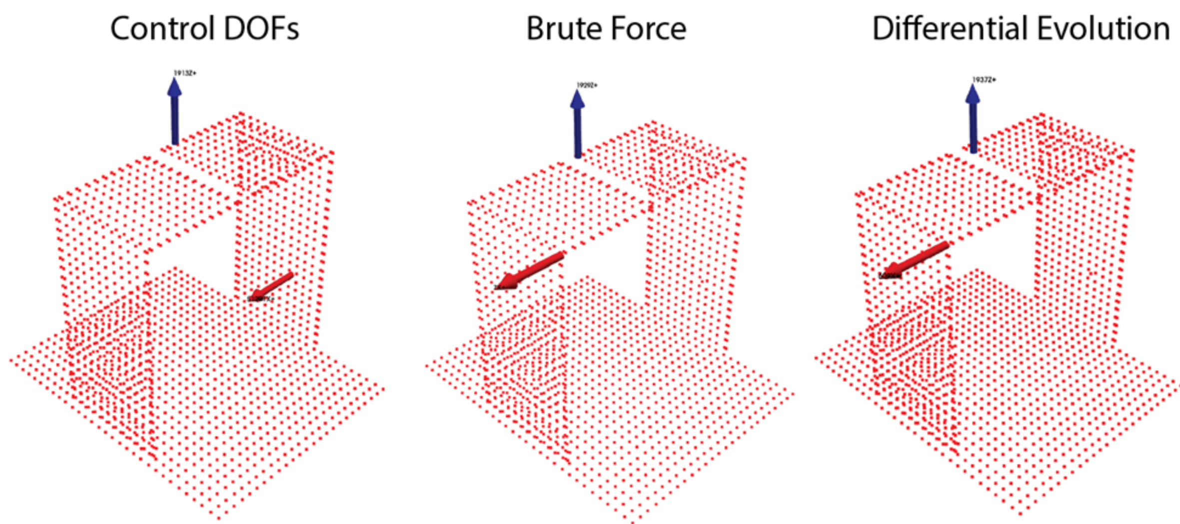

Fig. 14 Control DOFs (left), optimal candidate DOFs from Brute Force (middle), and optimal candidate DOFs from Differential Evolution (right).

Environmental Testing

For environmental testing, we slightly altered the test setup from the impact test configuration. The original rubber bands used for the impact test could not be used due to stretching, so they were replaced. We selected replacement rubber bands based on approximate similarity to the original rubber bands because we aimed to replicate the system that was characterized in the impact test. Similarly, two shakers (The Modal Shop K2007E01) were suspended from the test frame on bungees to decouple them from the flexible modes of the test stand. This decoupling is particularly important in the context of shaker placement optimization because our optimization algorithm did not account for the interaction between shaker and frame as a function of location.

We implemented random vibration MIMO tests in two configurations for this study. The first configuration used engineering judgment to collocate the two shakers with the two control DOFs. Intuitively, this configuration reflected the optimization priorities of matching the auto PSD at the two control DOFs while minimizing shaker force. The second configuration used the shaker DOFs found by the optimization algorithm. Figure 15 shows the configuration for each test. A gain of 18dB was prescribed for the shakers during both test configurations.

We used the Rattlesnake Vibration Controller software, an open-source Python software developed by Sandia National Laboratories, coupled with National Instruments data acquisition hardware to control multiple shakers during testing [13]. For all tests, we used a built-in controller called *buzz control* with a 50% overlap Tukey window, a constant overlap and add (COLA) time series generator, and a 20-frame (average of 20 seconds) dynamic spectral density matrix estimation.

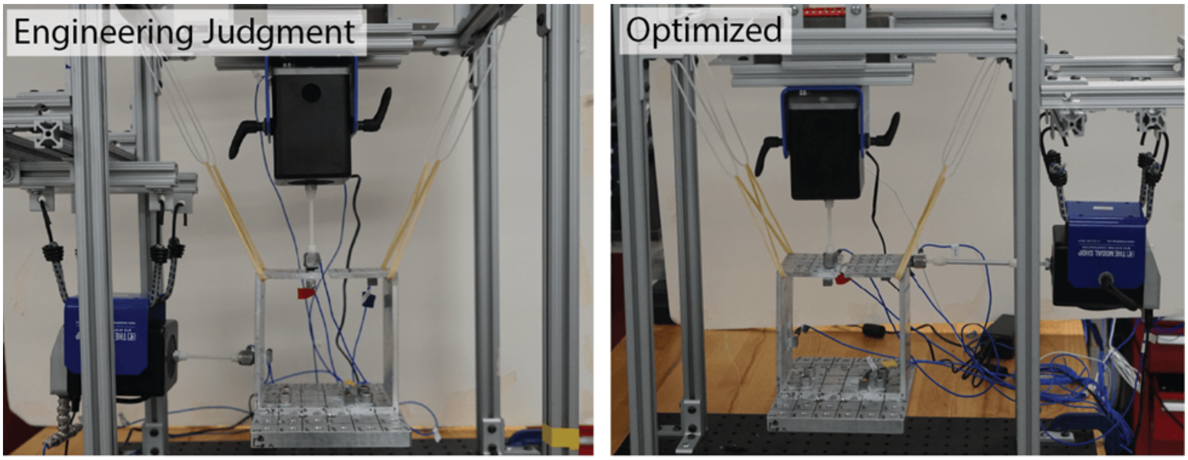

Fig. 15 Hardware test configurations for the engineering judgment setup (left) and optimized setup (right).

Sampling was set at 1800 Hz with a frequency line spacing of 1 Hz to align the frequency lines of the dynamic estimation with that of the specification. The Rattlesnake controller performs a system identification step for each test to re-estimate transfer functions between shaker voltage and control DOF acceleration. The buzz control algorithm then uses the in-situ measurements from the system identification step to populate the cross powers in the specification. Test data were collected for 2 minutes for each test.

Analysis

Before comparing the two tested configurations (engineering judgment and optimized), it is useful to describe relevant error metrics and their relative importance. In our application of random vibration testing, the "targets" are control auto PSDs at specified DOF. Our target auto PSDs and measured test auto PSDs are vectors with one value per frequency line, but it is often useful to reduce test performance metrics to a single value for easier comparison [2]. We therefore consider vector error metrics described below as well as comparing RMS values between testing configurations.

In the Environmental Specification section, we described computing MPE auto PSDs for channels 97Z and 58X. We followed this same process to compute MPE auto PSDs for all other measured acceleration channels in the field data, for 12 auto PSDs total. These PSDs will be referred to as *field auto PSDs*. To compute a global error metric for all measured channels, we define the field auto PSD values as $s_{p,i}$, where p indicates the channel number ($p \in \{1, 2, \cdots, N\}$) and i indicates the frequency line ($i \in \{1, 2, \cdots, M\}$). Likewise, we define experimental auto PSD values as $\overline{s_{p,i}}$. For this study, we used 791 frequency lines and 12 acceleration channels, but the derivations will be presented for general N and M here. We concatenate these auto PSD values into $N \times M$ matrices $S_{N,M}$ and $\overline{S_{N,M}}$, defined as

$$S_{N,M} = \begin{bmatrix} s_{1,1} & \cdots & s_{1,M} \\ \vdots & \ddots & \vdots \\ s_{N,1} & \cdots & s_{N,M} \end{bmatrix}_{N \times M} \tag{9}$$

$$\overline{S_{N,M}} = \begin{bmatrix} \overline{s_{1,1}} & \cdots & \overline{s_{1,M}} \\ \vdots & \ddots & \vdots \\ \overline{s_{N,1}} & \cdots & \overline{s_{N,M}} \end{bmatrix}_{N \times M} . \tag{10}$$

We then compute the relative error matrix $R_{N,M}$ using these two matrices. We chose relative rather than absolute error to avoid over-weighting the highest amplitude channel, as errors tend to be proportional to excitation amplitude. $R_{N,M}$ is given by

$$R_{N,M} = \begin{bmatrix} \frac{\overline{s_{1,1}}}{s_{1,1}} & \cdots & \frac{\overline{s_{1,M}}}{s_{1,M}} \\ \vdots & \ddots & \vdots \\ \frac{\overline{s_{N,1}}}{s_{N,1}} & \cdots & \frac{\overline{s_{N,M}}}{s_{N,M}} \end{bmatrix}_{N \times M} . \tag{11}$$

The error values in $R_{N,M}$ still have widely differing magnitudes at any given frequency line based on the magnitude of the specification, so we next normalize the error metric to avoid over-weighting the lowest amplitude channel [2]. We define a normalizing vector η of length M, where each entry is the L2 norm of the specification magnitude at that frequency line:

$$\eta = \left[\|S_{1,1\rightarrow N,1}\| \quad \cdots \quad \|S_{1,M\rightarrow N,M}\| \right]_{1\times M}, \tag{12}$$

where, for each frequency line i,

$$\|S_{1,i\rightarrow N,i}\| = \sqrt{s_{1,i}^2 + \cdots + s_{N,i}^2}. \tag{13}$$

We then compute a weighting factor $W_{N,M}$ to be applied to the relative error:

$$W_{N,M} = \begin{bmatrix} \frac{s_{1,1}^2}{\eta^2} & \cdots & \frac{s_{1,M}^2}{\eta^2} \\ \vdots & \ddots & \vdots \\ \frac{s_{N,1}^2}{\eta^2} & \cdots & \frac{s_{N,M}^2}{\eta^2} \end{bmatrix}_{N\times M}. \tag{14}$$

Next, we define the the weighted relative error matrix $E_{N,M}$ as element-wise multiplication of $R_{N,M}$ and $W_{N,M}$:

$$E_{N,M} = \begin{bmatrix} R_{1,1}W_{1,1} & \cdots & R_{1,M}W_{1,M} \\ \vdots & \ddots & \vdots \\ R_{N,1}W_{N,1} & \cdots & R_{N,M}W_{N,M} \end{bmatrix}_{N\times M}. \tag{15}$$

Lastly, we sum $E_{N,M}$ across the N channels to obtain the global error vector G:

$$G = \left[\sum_{p=1}^{N} E_{p,1} \quad \cdots \quad \sum_{p=1}^{N} E_{p,M} \right]_{1\times M}. \tag{16}$$

With error metrics defined, we next present test results. We first compared the force auto PSD GRMS values between the two test configurations (engineering judgment and optimized). Figure 16 plots the force auto PSDs and reports the lbRMS (RMS of the signal in lb) value for each shaker. The optimized configuration resulted in a lower force lbRMS

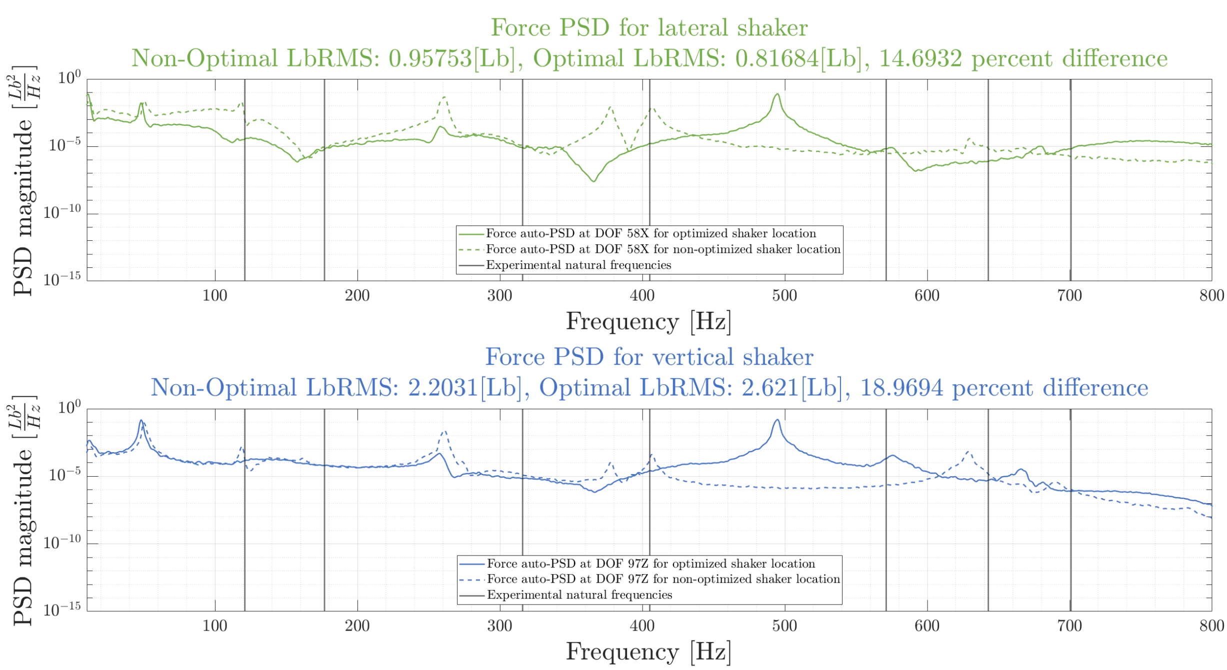

Fig. 16 Comparison of required force auto PSDs between optimized (solid) and non-optimized (dashed) shaker locations. The natural frequencies from experimental modal analysis are indicated by black vertical lines.

for the horizontal shaker, but a higher lbRMS for the vertical shaker. Averaging lbRMS results between both shakers, the engineering judgment test required less force than the optimized test.

After analyzing the measured force between configurations, we assessed measured acceleration in each test configuration. Figure 17 shows the auto PSDs at the two control locations compared to the specification for the engineering judgment shaker test. We observe the largest deviation from the specification around 350-400 Hz. The GMRS percent error between specification and test was 0.957% and 6.02% for the horizontal and vertical DOFs, respectively. Figure 18 shows the global

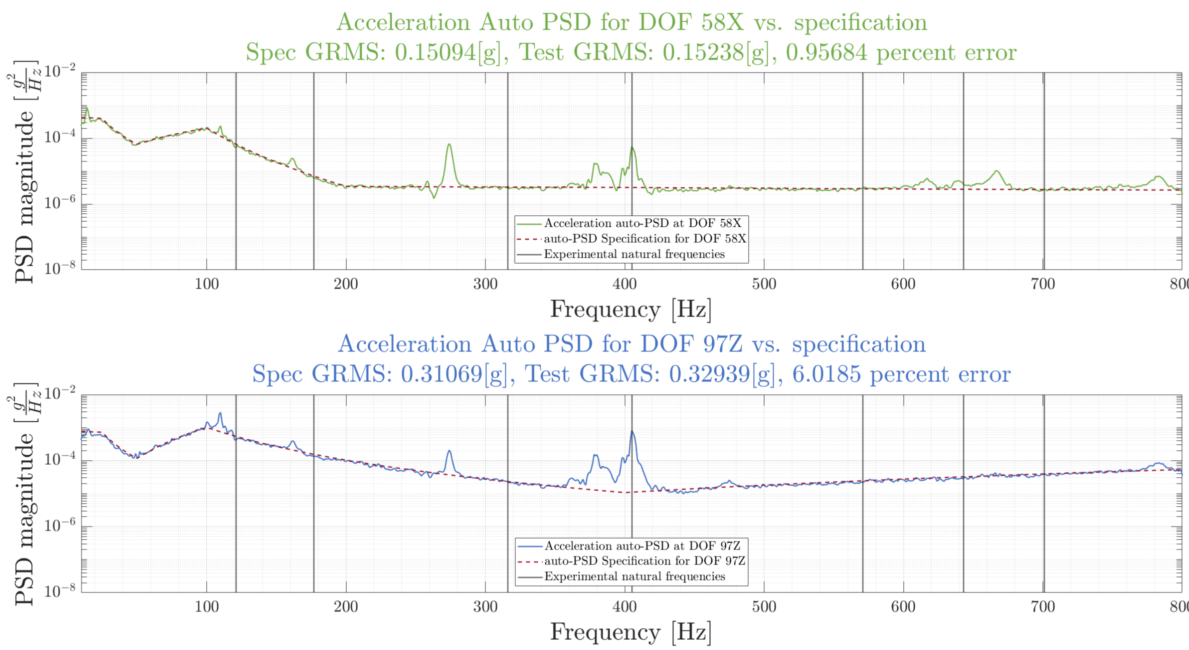

Fig. 17 Specification auto PSDs (red, dashed) and experimental auto PSDs (solid) for the engineering judgment test configuration. The natural frequencies from experimental modal analysis are indicated by black vertical lines.

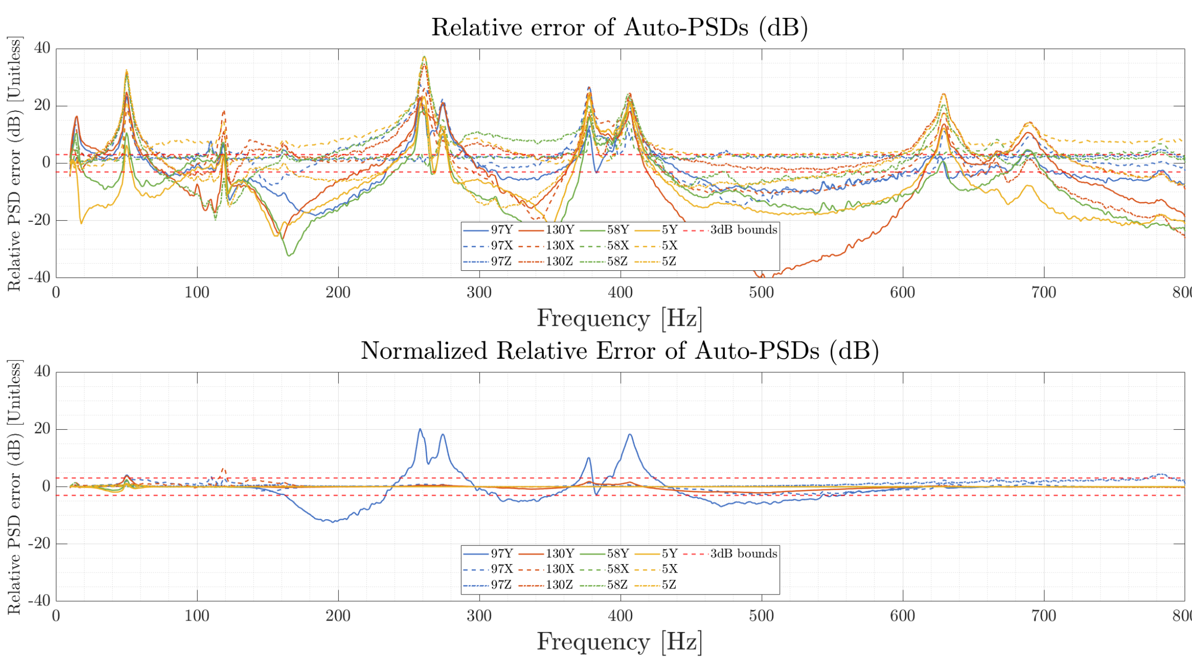

Fig. 18 Global relative error for all measured DOF for the engineering judgment test configuration.

relative error, both un-normalized and normalized, for all measured acceleration channels in the engineering judgment test. One interesting observation is that DOF 97Y has the highest normalized global error. This DOF could be an ideal control channel in future multi-input tests.

Next, we conducted the same analysis for the optimized test configuration. Figure 19 compares the auto PSDs between specification and test at the two control locations for the optimized shaker test configuration. Visually comparing these results to Figure 17, we observe a smaller deviation from the specification in the 350-400 Hz range, but a larger deviation from 700-800 Hz. The GMRS percent error between specification and test was 9.15% and 4.29% for the horizontal and vertical DOFs, respectively. By this GRMS metric, the optimized shaker location performed worse for the horizontal DOF and slightly better for the vertical DOF. Averaging across control channels, the engineering judgment test produced better control performance. Figure 20 shows the un-normalized and normalized global relative error for all measured acceleration channels in the optimized test. Just as with the engineering judgment test, DOF 97Y has the highest normalized global error.

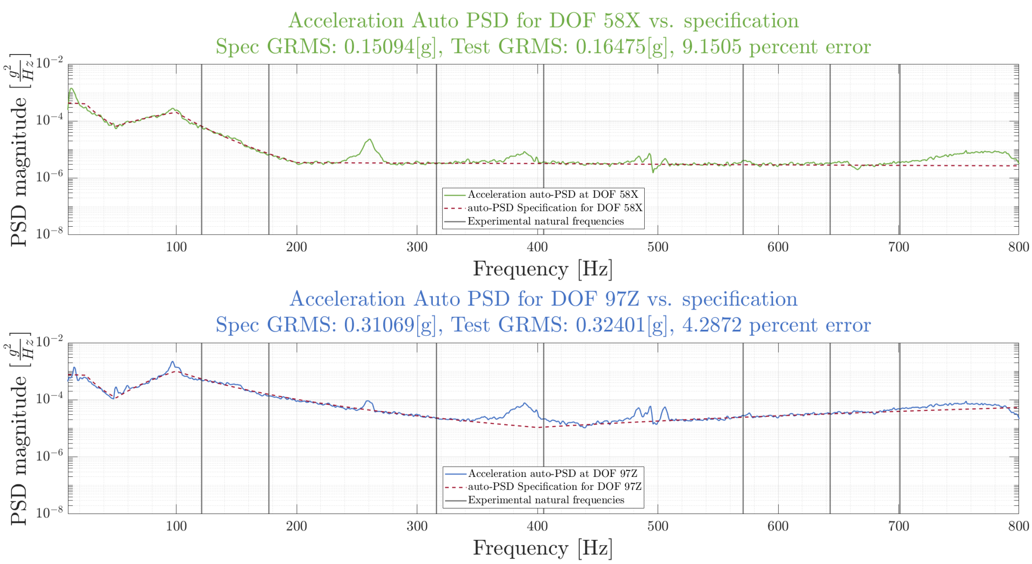

Fig. 19 Specification auto PSDs (red, dashed) and experimental auto PSDs (solid) for the optimized test configuration. The natural frequencies from experimental modal analysis are indicated by black vertical lines.

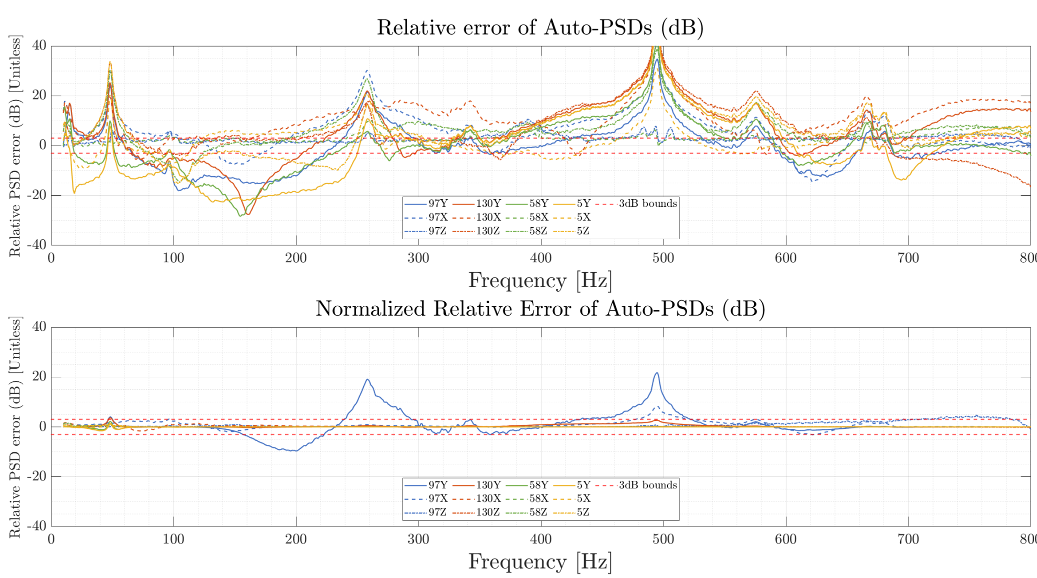

Fig. 20 Global relative error for all measured DOF for optimized shaker locations

Discussion

The optimization algorithm implemented in this study aimed to minimize shaker force while matching the specifications at the two control DOFs. However, our analysis revealed that the optimized shaker locations required more force than the engineering judgment configuration, as calculated by the sum of the lbRMS across the two shaker input force auto PSDs. This result was particularly surprising because the optimized shaker DOFs were located on the most flexible part of the structure. Additionally, the optimized shaker locations performed worse with respect to average error from test specification auto PSDs.

Potential sources of error for the force auto PSDs include a lack of modeling of the impedance associated with the shakers, lack of modeling of suspension stiffness, and shakers not being perfectly aligned during testing. Additionally, failing to model system damping in the FEA model may have contributed to increased error. Figure 21 shows sample FRFs between 58X and 97Z from the FEA model, experimental modal analysis, and environmental test. Visually, the addition of the shakers causes a large change in the FRF, contributing to the discrepancy between FEA optimization and hardware.

Notably, the first two modes were similar in frequency and magnitude across all three FRFs in Figure 21, but it is unclear whether this trend holds true across all the FRFs in the optimization search space. We were unable to run a comparison of all FRFs because we only tested two shaker test configurations. However, it is reasonable to assume that the addition of shakers in any test configuration would create differences between hardware and FEA FRFs. In Figure 21, the impact test and FEA FRFs are more similar, which is to be expected because we updated the FEA model to match impact test results. It is unclear how best to estimate the effect of shaker impedance during the optimization, but the discrepancy between the impact test FRFs and shaker test FRFs indicate that this consideration is crucial for effective shaker placement optimization.

The decrease in control performance with the optimized shaker locations (Figure 17 versus Figure 19) is similarly notable. The shakers used in this study had three gain settings. Depending on the transfer function between input voltage and output acceleration, any gain setting could simultaneously be too high for a given frequency line and too low for other frequency lines. For example, if an auto PSD specification at a given frequency line is 10^{-4} g^2/Hz while the transfer function magnitude at that frequency line is 10^{-6} g/V (as it might be at an anti-resonance), the gain would need to be set around 20 dB to keep the control signal between the desired bounds of $\pm 1V$. However, if that same auto PSD specification continued to a frequency line where the transfer function magnitude was 10^{-4} g/V (such as at a mode), a gain of 20dB would be excessive. The optimized shaker configuration produced different transfer functions between shaker and control DOFs, and our choice gain settings may have contributed to the over-test from 700-800 Hz, resulting in higher GRMS error.

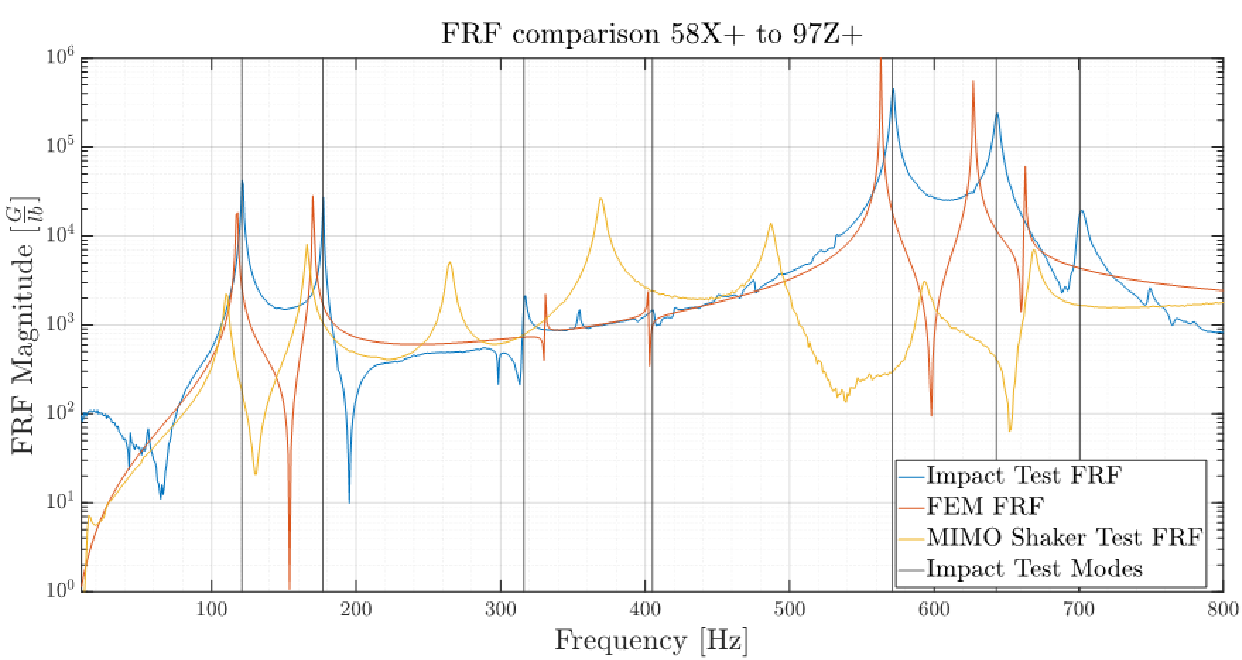

Fig. 21 FRFs computed between DOFs 58X and 97Z from the impact test, finite element analysis, and MIMO shaker test. The black vertical lines show the frequency values of the modes from the impact test.

Additionally, rigid body motion likely deflected shakers relative to the BARC and caused some bending in the stingers. This behavior could have created non-measured shear and moments applied to the structure, thus impacting the control performance. The rigid body motion could be addressed in future work through improved control algorithms for low frequencies, better experimental practices, or changing the testing range of interest.

Conclusions

The results from this study indicate that our optimization formulation, which minimized GRMS shaker force while matching the auto PSD specification at two control DOFs, was not effective when applied to the FEA model of the BARC base and plate. We found several reasons that explain the poor performance.

First, we observed differences in peak location and amplitude in the FRFs between FEA model, experimental modal analysis, and in-situ conditions during the environmental test (Figure 21). We certainly expected differences between model and hardware, but the discrepancy observed in this study was large enough to make an optimization with FEA FRFs effectively useless in the hardware test. We intentionally ignored the shaker impedance in the FEA model due to time constraints, but its omission led to an inaccurate system characterization.

Second, our transportation environment had a lower frequency bound of 10 Hz. The large displacements caused by low-frequency excitation most likely led to shear/moment transfer through the shaker stingers. The applied moments led to control error, which we believe is related to the increase in force. Across our tests, increased control error was correlated with increased lbRMS requirements.

Future work could investigate higher fidelity FEA modeling, such as the inclusion of shakers in the FEA model. The challenge with including shaker models in a shaker placement optimization is that the shaker locations and directions are not known a priori, so the system FRFs would have to be updated on each optimization iteration. However, this added computation may be worthwhile given the differences in FRFs between FEA and hardware observed in this study.

Another suggestion for future work is to explore changes in the search space of the optimization algorithm, such as incorporating non-normal excitation directions. Furthermore, the sensitivity of optimization results to spatial discretization in the search space could be explored. As the efficiency of search algorithms depends on the size of the search space, investigating what degree of model fidelity meaningfully contributes to results could aid in the application of shaker placement optimization to more complex assemblies than the BARC.

Additionally, new optimization problems could be explored. In this study, we notably did not consider the cross power spectra in the optimization problem. Our cost and constraints focused on matching the auto PSDs at control DOFs while minimizing force. Future work could consider the achievability of cross power spectra, include more control DOFs than shakers, or consider the response at non-control DOFs. A more sophisticated algorithm could account for variable-sized shakers, which would be useful for environments where there are large differences in specification magnitude between axes.

With respect to test implementation, test setup and control algorithm strategies for low frequency environments could be improved to reduce error associated with shear/moment transfer from stingers. Increasing the minimum frequency cutoff of the environmental specification addresses this error at the cost of misrepresenting the environment. In transportation environments, for example, the low-frequency, high-displacement motion is important to include for qualification tests. Improved experimental strategies could include the selection of flexible stingers to avoid transferring force or active control of shaker position to match the low frequency displacements of the device under test.

This project investigated the use of shaker placement optimization based on FRFs from an updated FEA model in multi-input environmental testing and found that additional considerations, such as shaker impedance and control of low frequency environments, must be considered to make optimization algorithms effective. Our results provide a valuable benchmark for test engineers that use FEA models for multi-input environmental test planning.

Acknowledgments This research was funded by Los Alamos National Laboratory (LANL) through the Engineering Institute's Los Alamos Dynamics Summer School. The Engineering Institute is a research and education collaboration between LANL and the University of California San Diego's Jacobs School of Engineering. This collaboration seeks to promote multidisciplinary engineering research that develops and integrates advanced predictive modeling, novel sensing systems, and new developments in information technology to address LANL mission-relevant problems. The authors would also like to thank Siemens for their donation of their Simcenter Testlab software for use in this project and Thomas Thompson from LANL for his advice on specification development. LA-UR-24-30459.

References

1. *Department of Defense Test Method Standard for Environmental Engineering Considerations and Laboratory Tests* (2000)
2. Hoksbergen, J. “Defining the global error of a multi-axis vibration test”. *Sound and Vibration*, 48:8–13 (2014)
3. Daborn, P.M. “Smarter dynamic testing of critical structures” (2014)
4. Pak, C.G. “Multiple shaker placement for ground vibration test of x-59 aircraft using topology optimization”. *NASA Armstrong Flight Research Center* (2020)
5. Rohe, D.P., Nelson, G.D., and Schultz, R.A. “Strategies for shaker placement for impedance-matched multi-axis testing”. In Walber, C., Walter, P., and Seidlitz, S., editors, *Sensors and Instrumentation, Aircraft/Aerospace, Energy Harvesting & Dynamic Environments Testing, Volume 7*, pages 195–212, Cham (2020) Springer International Publishing.
6. Rohe, D.P., Schultz, R., and Hunter, N. *Rattlesnake User’s Manual*. Sandia National Lab. (SNL-NM), Albuquerque, NM (United States), United States (2021)
7. Schultz, R.A. and Nelson, G.D. “Input signal synthesis for open loop multiple-input/multiple-output testing”. *Society of Experimental Mechanics* (2020)
8. Natrella, M.G. *Experimental Statistics*. National Bureau of Standards (1963)
9. Cap, J.S. “A tutorial on analysis techniques for deriving mechanical shock and vibration environmental specifications from field data”. *Society of Experimental Mechanics* (2021)
10. Lytle, T., Saeger, W., Tombuelt, A., Danforth, S., DeCleck, J., Ouellette, B., and Schultze, J. “Evaluating vibration controller performance in virtual and hardware tests”. In *Proceedings of the International Modal Analysis Conference XLII*. Society for Experimental Mechanics (2024)
11. Slater, J. “Examining spatial (grid) convergence” (2021)
12. Rohe, D. “Sdynpy: A structural dynamics python library”. In *Proceedings of the International Modal Analysis Conference XLI*. Society for Experimental Mechanics (2023)
13. Rohe, D., Shultz, R., Hunter, N., CERTTECH, and USDOE. *Rattlesnake Vibration Controller v.2.0*. Sandia National Lab. (SNL-NM), Albuquerque, NM (United States), United States (2021)
14. Berens, P. “Circstat: A matlab toolbox for circular statistics”. *Journal of Statistical Science*, 31 (2009)

Appendix: Cross Powers from Field Data

In this study, we focused on the auto PSDs for specification development and multi-input test control. However, we also derived specifications for the cross power spectral density, referred to as the “cross power” or “cross PSD” in this appendix, between the two control DOFs. This appendix describes the derivation and result for the interested reader.

In the Environmental Specification section, we computed the auto PSDs S_{xx} and S_{yy} for signals x and y, respectively. We use these quantities to compute the coherence γ_{xy} at each frequency value ω_i ($i \in \{1, 2, \cdots, M\}$ for M frequency lines) for signal block N_j ($j \in \{1, 2, \cdots, P\}$ for P signal blocks):

$$\gamma_{xy}(\omega_i, N_j) = \frac{|S_{xy}(\omega_i, N_j)|^2}{S_{xx}(\omega_i, N_j) * S_{yy}(\omega_i, N_j)}. \tag{17}$$

Using the computed coherence, the magnitude of the cross power $|S_{xy}|$ is given by

$$|S_{xy}(\omega_i, N_j)| = \sqrt{\gamma_{xy}(\omega_i, N_j) S_{xx}(\omega_i) S_{yy}(\omega_i)}. \tag{18}$$

Recall in the Environmental Specification section that we computed the Maximum Predicted Environment (MPE) for the auto PSDs at the control DOFs. To compute the cross power relative to those MPE auto PSDs $S_{xx}^{MPE}(\omega_i)$ and $S_{yy}^{MPE}(\omega_i)$, we can relate the matrix of auto PSD magnitude with cross PSD magnitude by computing conservative “worst case” amplitude estimates for the auto power magnitude and using the definition of coherence. This coherence-defined relationship between auto power and cross power magnitude is important because a coherence greater than 1 is not physically realizable.

$$|S_{xy}(\omega_i)| = \sqrt{\gamma_{xy}(\omega_i, N_j) S_{xx}^{MPE}(\omega_i) S_{yy}^{MPE}(\omega_i)}. \tag{19}$$

This leaves the coherence as the only remaining matrix. Unlike the auto PSD, where the “worst case loading” at each frequency line is a large PSD magnitude, the “worst case” for coherence is unclear. Therefore, we used the mean of the coherence as a reasonable approximation for a cross PSD magnitude that corresponds to the MPE auto PSD:

$$|S_{xy}(\omega_i)| = \sqrt{\overline{\gamma_{xy}}(\omega_i) S_{xx}^{MPE}(\omega_i) S_{yy}^{MPE}(\omega_i)}. \tag{20}$$

Computing the phase of the cross PSD is an additional challenge. For this study, we used the mean phase as computed with the CircStat Matlab toolbox[14]. We computed individual phase values from individual time blocks using Matlab’s

CPSD function, then inserted the phase values into the circular statistics mean estimator of CircStat. This process generated a set of phases, $\theta(\omega_i)$, for $i \in \{1, 2, \cdots, M\}$ frequency lines. After the cross PSD magnitude and phase are computed, we recombine them into the complete cross power, given by

$$S_{xy}(\omega_i) = |S_{xy}(\omega_i)| * e^{i\theta(\omega_i)}. \tag{21}$$

Figure 22 shows an example histogram of the cross PSD phase between the two control DOFs at one frequency line.

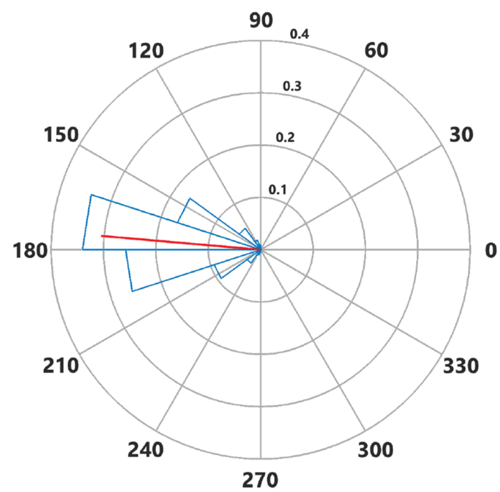

Fig. 22 Histogram for cross PSD phase at 340Hz between DOF 97Z to DOF 58X.

After computing the cross powers between the control DOFs, we assemble the spectral density specification matrix. Figure 23 shows the auto and cross PSDs computed for the two control DOFs in this study.

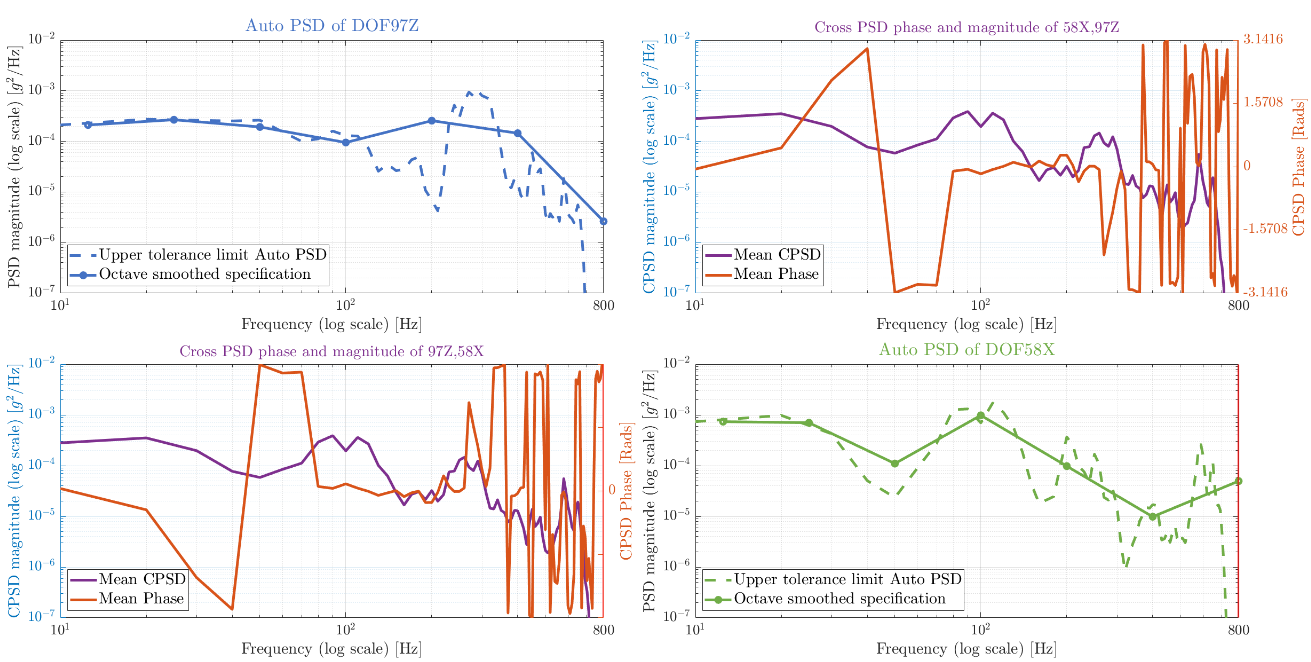

Fig. 23 MPE (P95/50) specification auto and cross PSDs for control DOFs 97Z and 58X.